ARTICLE

Check for updates

Characterization of oriented microstructures through anisotropic small-angle scattering by 2D neutron dark-field imaging

Jacopo Valsecchi [1,2✉], Markus Strobl[1,3], Ralph Patrick Harti[1,2], Chiara Carminati[1], Pavel Trtik[1], Anders Kaestner[1], Christian Grünzweig[1], Zhentian Wang[4,5], Konstantins Jefimovs[4,5] & Matias Kagias[4✉]

Within neutron imaging, different methods have been developed with the aim to go beyond the conventional contrast modalities, such as grating interferometry. Existing grating interferometers are sensitive to scattering in a single direction only, and thus investigations of anisotropic scattering structures imply the need for a circular scan of either the sample or the gratings. Here we propose an approach that allows assessment of anisotropic scattering in a single acquisition mode and to broaden the range of the investigation with respect to the probed correlation lengths. This is achieved by a far-field grating interferometer with a tailored 2D-design. The combination of a directional neutron dark-field imaging approach with a scan of the sample to detector distance yields to the characterization of the local 2D real-space correlation functions of a strongly oriented sample analogous to conventional small-angle scattering. Our results usher in quantitative and spatially resolved investigations of anisotropic and strongly oriented systems beyond current capabilities.

[1] Laboratory for Neutron Scattering and Imaging, Paul Scherrer Institut, 5232 Villigen, Switzerland. [2] University of Geneva, Geneva, Switzerland. [3] University of Copenhagen, NBI, Copenhagen, Denmark. [4] Laboratory for Macromolecules and Bioimaging, Paul Scherrer Institut, 5232 Villigen, Switzerland. [5] Institute for Biomedical Engineering, University and ETH Zurich, 8092 Zurich, Switzerland. ✉email: jacopo.valsecchi@psi.ch; matias.kagias@psi.ch

Neutron imaging is a nondestructive technique, which is able to probe bulk objects providing information about their internal structure with macroscopic resolution. In contrast to X-ray radiation, neutrons are sensitive to some light elements such as hydrogen and lithium, while they can penetrate many heavy elements, e.g. lead, according to the specific neutron cross sections[1,2]. Due to their intrinsic properties, imaging techniques based on neutron beam became versatile tools in many research fields, such as observation of water distribution in fuel cells, soil-root systems, geomaterials, mapping the elemental composition of fuel pellets and resolving magnetic properties in bulk samples[3–8]. A groundbreaking contribution to the imaging research field came with the development of the grating interferometry technique (GI) around two decades ago, with both X-ray (xGI) and neutron (nGI) radiations[9–16]. The GI approach yields simultaneously three different and complementary contrast signals: the transmission image (TI), the differential phase contrast image (DPCI) and the ultra-small-angle scattering referred as the dark-field image (DFI)[17]. Since its establishment, the nGI technique created significant impact in neutron imaging research, opening the way to probe and characterize different features of distinct materials in a wide variety of applications that were otherwise inaccessible. The first nGI experiment yielded to the visualization and quantification of the phase shift induced by nuclear interaction probed by DPCI[14]. A decade later the phase shift induced by the magnetic potential was measured by means of a grating interferometer in combination with polarized neutrons (pnGI)[18]. Even a concept to address fundamental physics problems such as the measurement of the neutron electric charge neutrality employing a Talbot-Lau interferometer in a high-intensity pulsed neutron beam has been proposed[19]. However, most of the investigations carried out with nGI have mainly focused on the small-angle scattering information provided by the DFI[20]. This contrast modality provides information on the microstructures of the sample on (sub)micrometer length scales, beyond the resolution capability of conventional neutron imaging[21–25]. A major breakthrough for the development of this approach could be established with the pursuit of quantitative evaluation of the neutron dark-field signal providing information about the macroscopic variations of the microstructure[26–29]. Furthermore, the DFI contrast proved to be a powerful tool for the investigation of magnetic domains in particular in bulk ferromagnetic grain-oriented electrical steels and of magnetic phenomena in superconductors as well[30–40]. Another important application field of DFI is related to the porosity and early crack formation detection in engineering materials, becoming particularly important in additive manufacturing studies[23,41].

Remarkable efforts have been put in place to develop the nGI technique, improving the instrumentation quality and pushing the boundaries of the accessible length scales toward the hundreds of nanometers range[42–48]. Besides providing information about the characteristic microscopic structure sizes in the probed object, the dark-field signal due to the underlying small-angle scattering (SAS) is sensitive to structural anisotropy and orientation. However, standard nGI measurements are based on line gratings which imply SAS sensitivity only perpendicular to the grating lines[49].

Within the X-ray community, the earlier implementations to achieve directional sensitivity were based either on rotating the interferometer setup or the sample[50,51]. Furthermore, different approaches including new grating designs, such as checkerboard and speckle patterns paved the way for further developments[52–59]. Among all the disparate grating geometries the circular design has been implemented to characterize the transverse coherence of X-ray beams, demonstrating the advantages of this solution, and opened up the possibility for additional applications[60].

In order to overcome this limitation in directional sensitivity, here we demonstrate a broadband, single-shot imaging approach with 2D dark-field SAS resolution based on a neutron far-field interferometer characterized by a grating design consisting of small pitch circular gratings arranged into a square array.

To achieve single-shot imaging the interference pattern generated by the diffractive phase grating is directly resolved on the high-resolution neutron detector, without requiring an absorbing analyzer grating. An angle dependent local fringe analysis is then performed to retrieve the local directional dark-field signal of the sample for each independent circular array of the modulation pattern. The grating design can be understood as a 2D periodic repetition of a circular unit cell. This is in analogy to a circular grating interferometry approach introduced at highly coherent synchrotron radiation and eventually generalized to polychromatic and incoherent X-ray sources by redesigning the unit cell[61,62]. Here, we adapted the circular grating interferometer idea for application with a cold neutron beam. Furthermore, we extend the approach towards spatially resolved quantitative 2D-SAS analyses and structural characterization. In order to achieve this we varied the sample to detector distance (L_s), varying accordingly the autocorrelation length (ξ) probed by each specific measurement, which is thus enabling a systematic quantitative scattering study of the locally strongly oriented system, in analogy to the case of isotropic microstructure characterization established in refs. [27,28].

Results

Working principle of the 2D-Diffractive far-field neutron grating interferometer. The neutron interferometer is composed by an absorbing source grating (G_0) and a phase shifting grating (G_1). A schematic of the circular unit cell nGI setup is depicted in Fig. 1a. Despite the presented method does not intrinsically rely on coherent illumination, conventional neutron beams usually do not provide sufficient collimation in order to observe the interference pattern. Therefore, an absorbing source grating is required in order to create an interference pattern at the detector distance which leads to the condition[62]:

$$g_0 < \frac{(l + d)}{2dp_1}, \tag{1}$$

where g_0 is the beam aperture, which corresponds to the holes diameter of the 2D array as described in the Method section and shown in Fig. 1a. The parameter l corresponds to the distance between the two gratings, d is G_1 to detector distance and p_1 the annular periodicity of G_1 as depicted in Fig. 1. The 2D pinholes array geometry of G_0 is designed such that a superimposition of the individual generated patterns corresponding to each aperture is achieved (Lau condition)[63].

Each unit cell of the phase grating G_1 is composed by one or more concentric annuli containing a diffractive substructure. The design of the phase grating G_1 is characterized by three periodicities: a global one W_1 and two local ones p_1 and g_1. W_1 corresponds to the repetition period of a unit cell as shown in Fig. 1a, b. The coarse local period p_1 corresponds to the annular period of the diffractive annuli, as mentioned above. Finally, the fine local period g_1 corresponds to the periodicity of the diffractive circular structure of the phase shifting annuli shown in detail in Fig. 1c.

The distance (d), depicted in Fig. 1a, between G_1 and the detector can be calculated, in the non-parallel beam case, as:

$$d = \frac{lz}{l - z}, \tag{2}$$

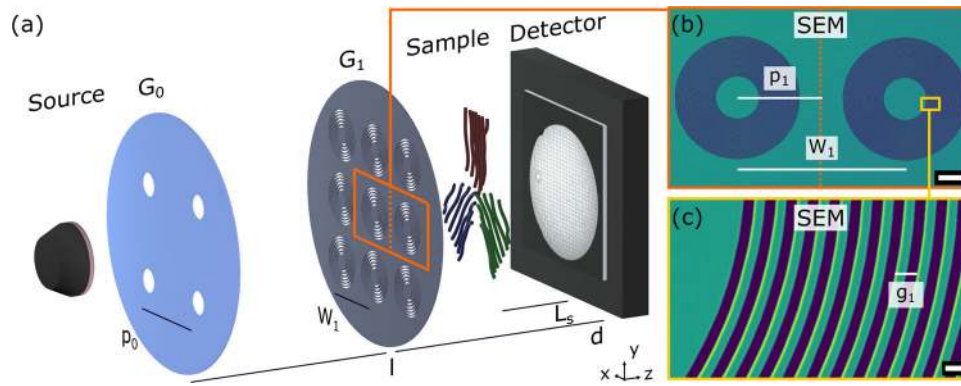where z equals to $\frac{p_1 g_1}{2\lambda}$, and λ the neutron wavelength.

Fig. 1 2D-Diffractive far-field neutron grating interferometer setup. a Schematic of the experimental setup. From left to right: the neutron source, the absorbing source grating G_O with its lattice constant p_0, the phase grating G_1 with its lattice constant W_1, the annular periodicity p_1 and the sample and the detector. G_1 is placed at a distance l from G_0, while d is the space in between G_1 and the detector. L_s is the sample to detector distance for the ξ-scan. The orientation of the sample fibers is color coded in blue, red and green, respectively to their angular displacement. The objects are depicted in a non-uniform scaling system. **b** Scanning electron microscopy (SEM) image of G_1 of two adjacent unit cells highlighted by the orange box, while the dashed line separates them. Scale bar, 50 μm. **c** SEM image of a unit cell portion depicted by the yellow box and its local periodicity g_1. Scale bar, 2 μm.

The global periodicity W_1 determines the projected experimental interference fringe matrix on the detector, which defines the spatial resolution of the retrieved dark-field signal with an effective pixel size corresponding to a single unit cell. The recorded pattern for each unit cell, assuming uniform diffraction properties of the circular grating in the range of one unit, can be approximated as a radial cosine function expressed in polar coordinates as:

$$I(r,\omega) = A\left[1 + V(\xi,\omega)\cos\left(2\pi\frac{r}{p_1}\right)\right], \qquad (3)$$

where A corresponds to the average intensity of the modulation pattern and $V(\xi,\omega)$ the radial visibility as a function of the autocorrelation length ξ. Assuming an oriented fiber structure the angle dependent visibility reduction can be modeled at each angle ω as following[62,64]:

$$V(\xi,\omega) = b_0(\xi) + b_1(\xi)\cos(\omega - \phi_d), \qquad (4)$$

where b_0 corresponds to the average scattering intensity, b_1 the oriented component of the scattering function, and ϕ_d the direction of the underlying fibers structure. The ratio b_1/b_0 can be regarded the degree of anisotropy of such a system. A standard experiment requires the acquisition of two images: an open beam image without the sample and one with it. Once the set of images has been recorded each unit cell is identified with a segmentation algorithm from the open beam image. This segmentation parameters are afterward used as a mask for the sample image. The segmented units are subsequently analyzed individually in the context of the corresponding open beam segments. The reconstruction algorithm performs as a first step a 2D-Fourier Transform to each unit cell and then converts it from Cartesian coordinates to polar coordinates in order to analyze the angular variation of the visibility, which is encoded in the intensity of the second harmonic[62]. Hence, the data extraction is performed in a similar manner to conventional grating interferometry at each angle ω, i.e., the visibility reduction is given then by:

$$V(\xi,\omega) = \frac{V_s(\xi,\omega)}{V_f(\xi,\omega)} = \frac{\hat{I}_s(\mathbf{q}_{m,n} = \mathbf{q}_\omega^N)\hat{I}_f(\mathbf{q}_{m,n} = \mathbf{0})}{\hat{I}_f(\mathbf{q}_{m,n} = \mathbf{q}_\omega^N)\hat{I}_s(\mathbf{q}_{m,n} = \mathbf{0})}, \qquad (5)$$

where V_s and V_f are the radial sample and open beam visibility, respectively. The $\hat{I}(\mathbf{q})$ is the power spectrum, the subscripts s and f refer to the sample and to the open beam, respectively, with $\mathbf{q}_{m,n}$ being the scattering vector in Cartesian coordinates and $\mathbf{q}_\omega^N$

utilizing the polar representation, where N is the ration of the unit cell size W_1 and the coarse period p_1, which corresponds to two.

The range of sensitivity for the characterization of microstructures changes by varying the sample to detector distance as reported in ref. [26,28]. The relation between the probed autocorrelation length ξ and L_s can be expressed as:

$$\xi = \frac{\lambda L_s}{p_1} \qquad (6)$$

where p_1 also corresponds to the period of the concentric intensity pattern recorded on the detector. Therefore, by varying L_s directly implies a scan of the autocorrelation length for a constant wavelength at which the image is recorded. The angular and autocorrelation lengths dependencies of the dark-field signal yields to quantitative information about the locally strongly oriented system.

Scattering models of anisotropic and strongly oriented systems. Assuming that the scattering from a single point results into a 2D-Gaussian scattering intensity profile, in the specific case of a quasi-1D structure like such as long oriented fibers, the visibility reduction can be expressed as[64]:

$$V(\omega) = (1-\alpha) + \alpha\,\exp\left[-\frac{2\pi^2\sigma^2}{p_1^2}\right],$$
$$\sigma^2 = \frac{1}{2}(\sigma_1^2 + \sigma_2^2) + \frac{1}{2}(\sigma_1^2 - \sigma_2^2)\cos(2[\omega - \phi_d] - \pi) \qquad (7)$$

where α corresponds to the proportion of the beam that has been scattered, σ_1 and σ_2 the widths of the 2D-Gaussian distribution in the two axial directions.

In the studies presented in ref. [64], the directional DFI variations of fiber structures have been studied for weakly and strongly oriented orders with conventional xGI, inferring that in the former case a sinusoidal behavior is expected as a function of the angle, while the latter display a nonsinusoidal trend, peaked at the preferred scattering direction. In an analogous way we studied the directional DFI variations of strongly oriented system, however, additionally as a functions of the probed autocorrelation lengths.

The change in DFI signal as a function of ξ yields additional quantitative information about the microstructures underlying the system and can be expressed as[26]:

$$DFI(\xi) = e^{\Sigma t(G(\xi)-1)}, \qquad (8)$$

where Σ is the macroscopic scattering cross-section, t the sample

thickness and $G(\xi)$ is the one-dimensional projection of the autocorrelation function of the scattering structure calculated via the Abel transform of the autocorrelation function. The macroscopic scattering cross-section is defined as:

$$\Sigma = \lambda^2 (\Delta\rho)^2 \zeta(1-\zeta)\chi, \tag{9}$$

where $\Delta\rho$ corresponds to the difference in scattering length density of the scatterer and the medium. ζ represents the volume fraction of the scatterer and χ its characteristic size. Different models have been derived in order to describe $G(\xi)$, in particular for the case of oriented anisotropic system such as the infinitely long cylinder, having its side parallel to the x axis and its diameter in the zy-plane, the correlation $\gamma(r)$ and autocorrelation functions are given by[65]:

$$\gamma(r) = \frac{2}{\pi}\left[\cos^{-1}\left(\frac{r}{D}\right) - r\frac{\sqrt{D^2 - r^2}}{D^2}\right],$$
$$G(z) = \int_0^D \gamma(\sqrt{x^2 + z^2})dx, \tag{10}$$

where D is the cylinder diameter.

Dark-field 2D real-space analysis of carbon fibers. A carbon fiber plate scaffolded into a polymer resin was selected as a model sample to study the dark-field signal from a locally strongly oriented system, as shown in Fig. 2a, b. The specimen thickness is

1 mm. The fibers of the sample are uniformly oriented along one direction parallel to the face of the sheet, a scanning electron microscopy (SEM) image of the sample can be seen in Fig. 2b. The plate has been cut in three pieces and oriented along exemplary directions, as depicted in Fig. 2a: the red one at 0°, the green one at 120° and the blue one at 240° with respect to the vertical direction. The corresponding dark-field signal arising from the fibers depends on their orientation. Therefore, the Y-shaped pie chart arrangement of the cut pieces provides a 120° angular displacement of the fibers orientations in the imaging plane can be regarded serving as validation for our purposes. Figures 2c, d show the results of the measurement, performed at 4.1 Å and ξ equals to 0.3 μm probed correlation length.

The two images are the attenuation contrast image in Fig. 2c and the color coded directional DFI image ($DFI_{directional}$) in Fig. 2d.

The conventional attenuation based transmission image in Fig. 2c allows to identify the edges of three distinct regions within the field of view (FoV), but without providing any useful information about the fiber structure and its orientation. On the other hand, the color coded directional DFI image in Fig. 2d clearly shows the triple-fold orientation variation corresponding to the different sample regions.

The directional DFI has been retrieved from all the individual scattering images at different angles and in order to represent the fibers orientations from the most prominent scattering direction.
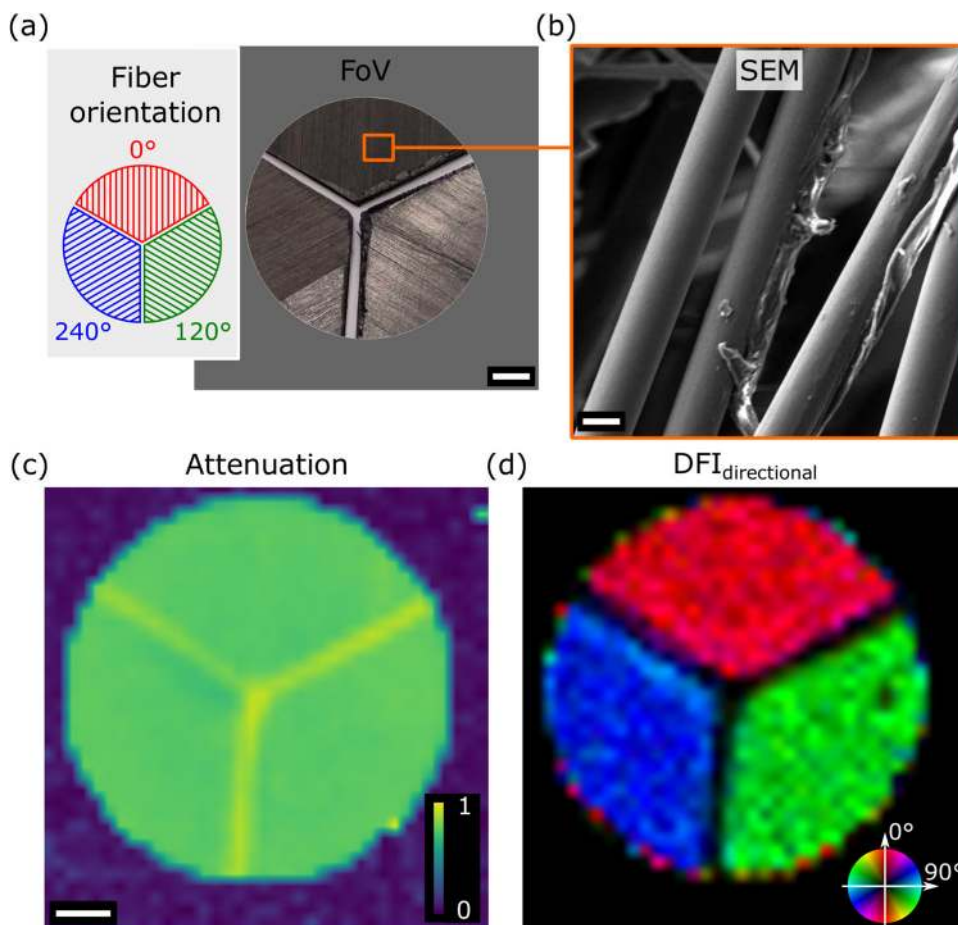

Fig. 2 Directional dark-field image of carbon fibers. a Photo of the measured carbon fiber sample within the field of view (FoV) oriented in Y-shaped pie chart angular displacement. The inset shows the sketch of the fibers orientation. Scale bar, 2 mm. **b** Scanning electron microscopy (SEM) image of the carbon fibers used in the experiment. Scale bar 5 μm. **c** Attenuation image. **d** Directional dark-field image $DFI_{directional}$. The hue saturation value (HSV) color wheel refers to the actual fibers orientation. A median filter with 3 × 3 kernel has been applied for visual representations. Panels **c** and **d** share the same scale bar, 2 mm, and have been measured at 4.1 Å, and at an autocorrelation length $\xi = 0.3$ μm.
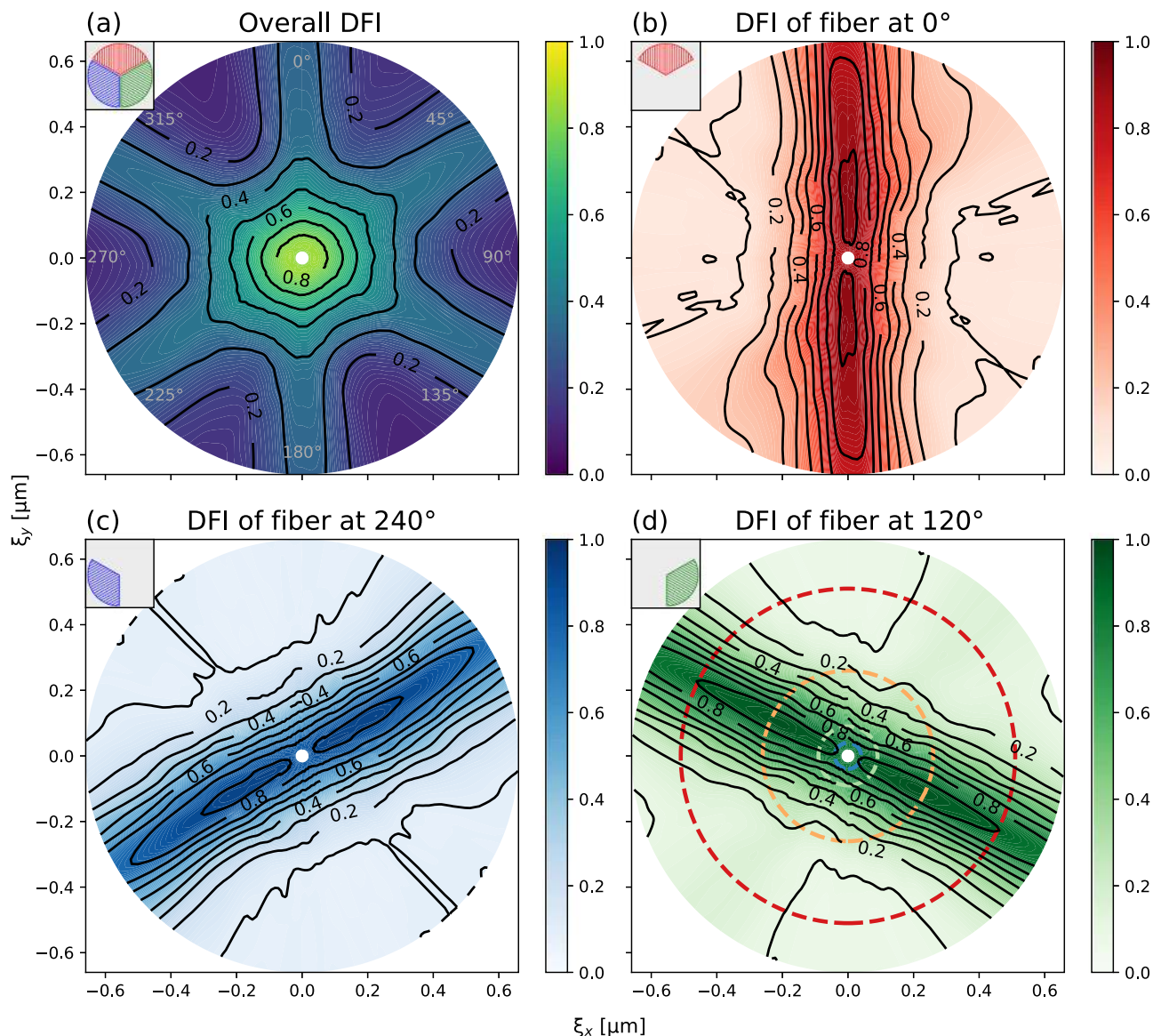
Fig. 3 Dark-field 2D real-space correlation functions. The Dark-field (DFI) 2D real-space correlation functions in Cartesian form retrieved through the sample to detector scan at 4.1 Å. The orthogonal coordinate system is express in terms of the autocorrelation lengths ξ_x and ξ_y in a similar manner as the small-angle neutron scattering (SANS) 2D-diffraction patterns. **a** DFI 2D real-space correlation function averaged over the whole field of view (FoV), averaging the scatting signal arising from the three different fibers orientations. The azimuthal angle, highlighted in gray, refers to ω. **b–d** Real-space correlation functions averaged over the segmented regions with diffident fibers orientations. The DFI 2D real-space correlation functions have been color coded in red for the 0° fibers orientation, green for the 120° and blue for the 240°, respectively. The four color coded concentric dashed circles in **d** refer to the contour lines at different autocorrelation lengths (0.04, 0.09, 0.26 and 0.51 µm). All the DFI 2D real-space correlation functions have been measured at 4.1 Å. The insets depict the four color coded different regions, within the FoV.

The directional information, including the scattering strength and the angle, encoded into the directional DFI uses the hue saturation value (HSV) color space in an analogous manner as adopted in refs. [61,62,64]. The hue corresponds to the characteristic direction of the oriented system; the saturation is set to 1 and the value is defined as the normalized amplitude of the scattering directionality, where the dark areas correspond to the ones with no directional scattering. In addition, our correlation length scans for quantitative SAS analyses were spanning a range from 20 nm to 670 nm as shown in Fig. 3. Figure 3a shows the 2D real-space correlation functions retrieved from our DFI data. The pattern in Fig. 3a is averaged over the whole FoV which is corresponding to the real space correlation function a conventional small-angle neutron scattering (SANS) measurement would yield, integrated

over the whole sample. In this representation of the results, Fig. 3a, we can draw some conclusions regarding the presence of three main orientations of the microstructures within the sample, nevertheless, without being able to properly identify if there is an orientation variation due to different regions or due to mixed fiber orientations throughout the sample. This is a common issue of conventional scattering methods when probing a non-homogeneous sample and the most widely adopted solution to tackle this problem is to perform a scanning pencil-beam SANS measurement in order to retrieve the spatially resolved scattering information, which is time consuming and cannot be performed in a single-shot acquisition. The results presented in the dark-field 2D real-space correlation functions of Fig. 3b–d show the directional dark-field signals averaged over the three segmented
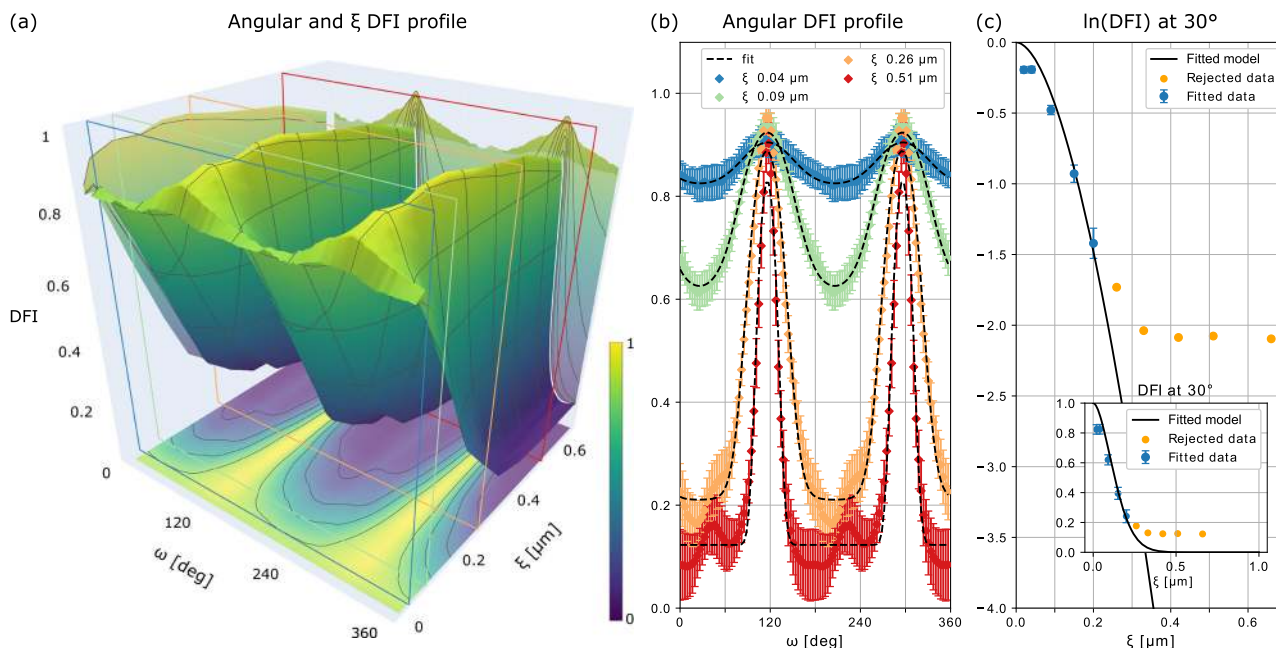
Fig. 4 Extracting the angular and the autocorrelation length dependence of the dark-field signal. a Dark-field (DFI) real-space correlation function expressed as a function of the angle ω from 0° to 360° and the autocorrelation length ξ from 20 nm to 670 nm. The color coded boxes highlight the cross-sections at four different autocorrelation lengths: 0.04 μm in blue, 0.09 μm in pale green, 0.26 μm in orange and 0.51 μm in red. **b** Angular dependence of the DFI signal for the four different color coded autocorrelation lengths depicted in **a**. The corresponding error bars are the standard error of the mean. Note the nonsinusoidal behavior of the orange and the red lines. The dashed black lines are model fits to the measured values. **c** Extracted real-space correlation function for the infinitely long cylinder model. The blue points have been used for the fitting while the orange ones have been rejected due to the saturation of the signal, clearly visible by the horizontal asymptotic behavior in the logarithm plot. The inset shows the DFI experimental points and the fitted model. The analysis refers to the 120° fibers orientation case.

Table 1 Fitted parameters for the fibers oriented at 120°, blue region, at four different autocorrelation length according to Jensen's 2D-Gaussian scattering model.

Autocorrelation length ξ (μm)	Fibers orientation (deg)	Fitted parameters			
		σ_1^2 [μm²]	σ_2^2 [μm²]	ϕ_d [deg]	α
0.04	120	75.7 ± 1.8	41.5 ± 1.2	116.5 ± 0.3	0.19 (±3.3%)
0.09	120	76.7 ± 1.2	22.5 ± 1.1	117.6 ± 0.3	0.42 (±3.1%)
0.21	120	132 ± 3.2	19.9 ± 1.1	116.3 ± 0.4	0.8 (±2.1%)
0.51	120	357 ± 15	23.5 ± 1.2	116.1 ± 0.3	0.87 (±2.8%)

The parameter uncertainties have been estimated as the standard deviation in the Levenberg-Marquardt fitting method.

areas in red for the 0° fibers orientation, green for the 120° and blue for the 240°, respectively, as depicted in the insets. The three dark-field 2D real-space correlation functions, Fig. 3b–d, clearly show highly eccentric scattering behaviors, for each region, parallel to the fibers orientation in the respective segmented areas, which is a distinct characteristic of strongly ordered systems.

Furthermore, the dark-field signal has been analyzed as a function of the angle and the autocorrelation lengths ξ, as shown in Fig. 4a, b.

The experimental results of the fibers, which exemplify a strongly oriented system, exhibit an angular dependency in terms of probed autocorrelation lengths, as shown in Fig. 4b, showing a sinusoidal behavior for shorter ξ and a nonsinusoidal one for longer ξ. Conventionally, this sinusoidal or nonsinusoidal behavior has been attributed to the orientation degree of the scatterer, for weakly and strongly oriented system, respectively, measured at a single specific sample to detector distance, as reported in ref. [64]. However, our case demonstrates how an

autocorrelation length scan combined with an analysis of the angular dependency is essential to make an assessment of the orientation degree of the scatterer. The experimental results have been fitted according to Eq. (7) showing good agreement with the model at four different autocorrelation lengths: 0.04 μm, 0.09 μm, 0.26 μm and 0.51 μm. The retrieved parameters σ_1^2, σ_2^2, ψ and α for all points are presented in Table 1. The parameters σ_1^2, σ_2^2 show an increment in the eccentricity of the 2D-Gaussian scattering profile as a function of the autocorrelation length.

Moreover, the consistency of ψ allows us to properly determine the angle of the fibers orientations at (116.6 ± 0.7)°, beyond a correction factor of ±180° due to phase wrapping.

As a last step of our investigation the experimental data have been described and fitted with the oriented infinitely long cylinder model according to Eqs. (8) and (10), as shown in Fig. 4c. Since the probed autocorrelation lengths ξ span from 20 nm to 670 nm and the diameter of the carbon fibers corresponds to 5 μm, as retrieved by means of the SEM image

in Fig. 2b, this characteristic size falls out of the probed range and hence cannot be fully assessed. Nevertheless, we can assume the diameter D, the volume fraction ζ values from SEM and use as a priori knowledge in order to calculate the macroscopic scattering cross-section Σ of Eq. (9) subsequently estimate the scattering length density contrast $\Delta\rho$.

Due to the saturation of the dark-field signal at longer autocorrelation lengths, which can be observed in the logarithmic representation of the dark-field value in Fig. 4c, a rejection threshold has been set in order to evaluate only the points with $\xi < 0.25$ μm. The composition of the sample can be approximated as carbon for the fibers (the scatter) and Hydrogen for the polymer resin (the medium), resulting into a $\Delta\rho = 49.537 \times 10^{-6}\,\text{Å}^{-2}$ for a wavelength of 4.1 Å[66]. The resulting scattering length density value from the fitting of the experimental points corresponds to $61 \pm 7.8 \times 10^{-6}\,\text{Å}^{-2}$ which is in reasonable agreement with the crude estimate and underlines the potential for quantitative analysis of our measurements.

Discussion

The authors have presented a neutron grating interferometer able to perform in a single-shot mode 2D directional dark-field image acquisition in addition to the conventional attenuation contrast. The single-shot approach in contrast to the existing methods does not require any rotation of the sample nor the gratings during acquisition compared to existing methods. The feasibility of the method was demonstrated by imaging a batch of carbon fibers oriented along three exemplary directions. The retrieved directional dark-field image clearly reveals the fibers orientations in the three distinct regions. Thus, the method achieves in a single step what was has been used to require several acquisitions previously. Furthermore we showed how the measurements at different correlation lengths, through the sample to detector scan, allow quantitative SAS analyses and the creation of a dark-field 2D real-space correlation function for every region of interest in the image. We demonstrated that the experimental results pave the way for further investigations leading to characterization and quantification of anisotropic microstructures, providing a model to fit the real-space correlation function and describing the fiber structure addressing the issue of signal saturation and how to circumvent the problem. The proposed method approaches the investigative strength of conventional scattering techniques, however, spatial resolution capabilities, and tremendously simplifies the access to multidirectional dark-field information enabling the study of non-homogeneous and anisotropic scattering from systems with preferred microstructural orientations such as in polymer science, soft condensed matter physics, rheological studies and nondestructive testing of additively manufacturing specimens.

Methods

2D-Diffractive far-field neutron grating interferometer setup. The validity of the proposed technique is demonstrated with experimental measurements conducted at the cold beamline ICON, at the Swiss Spallation Neutron Source (SINQ), at the Paul Scherrer Institut (PSI)[67]. A turbine based energy selector was used to get a monochromatic beam at a wavelength of 4.1 Åwith an energy resolution of $\frac{\Delta\lambda}{\lambda} = 12\%$. The source grating G_0 is a gadolinium sputtered absorbing mask positioned at the neutron beam aperture, it consists of 2D array of $g_0 = 1.3$ mm holes in an upright square lattice, with lattice constant $p_0 = 5.5$ mm, as shown in Fig. 1. A phase shifting grating (G_1) with a radial period p_1 of 300 μm and unit cell period g_1 of 2 μm was fabricated in house by e-beam lithography and etching of Si. The grating was etched to a depth of 37 μm, which at 4.1 Å produces a phase shift of π in the neutron wave packet. A scanning electron microscopy (SEM) image of the fabricated phase grating can be seen in Fig. 1b, c. In order to directly resolve the interference pattern on the detector a Fiber Optic Taper (FOT) has been adopted in combination with a 10 μm Gadox-based scintillator screen and a 100 mm objective, resulting into a spatial resolution of about 20 μm measured with a Siemens star test object[68,69]. The described nGI setup reaches a performance of 42% in visibility when combined with the velocity selector and around 20% with white beam. A total number of 55

directional dark-field images covering the range $[0, \pi]$ were retrieved from the single-shot measurements. The G_1 was placed at 7 m from the source grating G_0, whereas the detector at 0.4 m from G_1 according to Eq. (2). The sample was always placed in between the phase grating G_1 and the detector, as illustrated in Fig. 1a.

Data acquisition and reduction. A stack of 60 images, each with an exposure time of 320 s, has been reduced by median projection before applying the single-shot algorithm. The total acquisition time was mainly dictated by the flux reduction due to the velocity selector, the absorption grating G_0, and by the low light yield of the Gadox-based scintillator.

Data availability
The data that support the findings of this study are available from the corresponding author upon reasonable request.

References

1. Anderson, I. S. et al. Neutron imaging and applications. In *Neutron Scattering Applications and Techniques* (Springer, Boston, MA, 2009).
2. Kardjilov, N., Manke, I., Woracek, R., Hilger, A. & Banhart, J. Advances in neutron imaging. *Mater. Today* **21**, 652–672 (2018).
3. Boillat, P. et al. In situ observation of the water distribution across a PEFC using high resolution neutron radiography. *Electrochem. commun.* **10**, 546–550 (2008).
4. Kardjilov, N. et al. Three-dimensional imaging of magnetic fields with polarized neutrons. *Nat. Phys.* **4**, 399–403 (2008).
5. Carminati, A. et al. Dynamics of soil water content in the rhizosphere. *Plant Soil* **332**, 163–176 (2010).
6. Tremsin, A. S. et al. Non-destructive studies of fuel pellets by neutron resonance absorption radiography and thermal neutron radiography. *J. Nucl. Mater.* **440**, 633–646 (2013).
7. Forner-Cuenca, A. et al. Engineered water highways in fuel cells: radiation grafting of gas diffusion layers. *Adv. Mater.* **27**, 6317–6322 (2015).
8. Siegwart, M. et al. Distinction between super-cooled water and ice with high duty cycle time-of-flight neutron imaging. *Rev. Sci. Instrum.* **90**, 103705 (2019).
9. Momose, A. et al. Demonstration of x-ray Talbot interferometry. *Japanese J. Appl. Phys.* **42**, L866–L868 (2003).
10. Momose, A. Phase-sensitive imaging and phase tomography using X-ray interferometers. *Opt. Express* **11**, 2303–2314 (2003).
11. Weitkamp, T. et al. X-ray phase imaging with a grating interferometer. *Opt. Express* **13**, 6296–6304 (2005).
12. Momose, A. Recent advances in X-ray phase imaging. *Japanese J. Appl. Phys.* **44**, 6355–6367 (2005).
13. Pfeiffer, F., Weitkamp, T., Bunk, O. & David, C. Phase retrieval and differential phase-contrast imaging with low-brilliance X-ray sources. *Nat. Phys.* **2**, 258–261 (2006).
14. Pfeiffer, F. et al. Neutron phase imaging and tomography. *Phys. Rev. Lett.* **96**, 215505 (2006).
15. Pfeiffer, F. et al. Hard-X-ray dark-field imaging using a grating interferometer. *Nat. Mater.* **7**, 134–137 (2008).
16. Rauch, H. & Werner, S. A. *Neutron Interferometry*, 2nd ed. (Oxford University Press, 2015).
17. Endrizzi, M. X-ray phase-contrast imaging. *Nucl. Instrum. Methods Phys. Res.* **878**, 88–98 (2018).
18. Valsecchi, J. et al. Visualization and quantification of inhomogeneous and anisotropic magnetic fields by polarized neutron grating interferometry. *Nat. Commun.* **10**, 3788 (2019).
19. Piegsa, F. M. Novel concept for a neutron electric charge measurement using a Talbot-Lau interferometer at a pulsed source. *Phys. Rev. C* **98**, 45503 (2018).
20. Strobl, M. et al. Small angle scattering in neutron imaging—a review. *J. Imaging* **3**, 64 (2017).
21. Strobl, M. et al. Neutron dark-field tomography. *Phys. Rev. Lett.* **101**, 123902 (2008).
22. Strobl, M. et al. Differential phase contrast and dark field neutron imaging. *Nucl. Instrum. Methods Phys. Res.* **605**, 9–12 (2009).
23. Hilger, A. et al. Revealing microstructural inhomogeneities with dark-field neutron imaging. *J. Appl. Phys.* **107**, 36101 (2010).
24. Grünzweig, C. et al. Quantification of the neutron dark-field imaging signal in grating interferometry. *Phys. Rev. B* **88**, 125104 (2013).
25. Siegwart, M. et al. Selective visualization of water in fuel cell gas diffusion layers with neutron dark-field imaging. *J. Electrochem. Soc.* **166**, F149–F157 (2019).

26. Strobl, M. General solution for quantitative dark-field contrast imaging with grating interferometers. *Sci. Rep.* **4**, 7243 (2014).

27. Strobl, M. et al. Wavelength-dispersive dark-field contrast: micrometre structure resolution in neutron imaging with gratings. *J. Appl. Crystallogr.* **49**, 569–573 (2016).

28. Harti, R. P. et al. Sub-pixel correlation length neutron imaging: Spatially resolved scattering information of microstructures on a macroscopic scale. *Sci. Rep.* **7**, 44588 (2017).

29. Harti, R. P. et al. Visualizing the heterogeneous breakdown of a fractal microstructure during compaction by neutron dark-field imaging. *Sci. Rep.* **8**, 17845 (2018).

30. Grünzweig, C. et al. Bulk magnetic domain structures visualized by neutron dark-field imaging. *Appl. Phys. Lett.* **93**, 112504 (2008).

31. Grünzweig, C. et al. Neutron decoherence imaging for visualizing bulk magnetic domain structures. *Phys. Rev. Lett.* **101**, 025504 (2008).

32. Lee, S. W. et al. Observation of magnetic domains in insulation-coated electrical steels by neutron dark-field imaging. *Appl. Phys. Express* **3**, 106602 (2010).

33. Manke, I. et al. Three-dimensional imaging of magnetic domains. *Nat. Commun.* **1**, 125 (2010).

34. Rauscher, P. et al. The influence of laser scribing on magnetic domain formation in grain oriented electrical steel visualized by directional neutron dark-field imaging. *Sci. Rep.* **6**, 38307 (2016).

35. Betz, B. et al. In-situ visualization of stress-dependent bulk magnetic domain formation by neutron grating interferometry. *Appl. Phys. Lett.* **108**, 012405 (2016).

36. Harti, R. P. et al. Dynamic volume magnetic domain wall imaging in grain oriented electrical steel at power frequencies with accumulative high-frame rate neutron dark-field imaging. *Sci. Rep.* **8**, 15754 (2018).

37. Reimann, T. et al. Visualizing the morphology of vortex lattice domains in a bulk type-II superconductor. *Nat. Commun.* **6**, 8813 (2015).

38. Reimann, T. et al. Domain formation in the type-II/1 superconductor niobium: interplay of pinning, geometry, and attractive vortex-vortex interaction. *Phys. Rev. B* **96**, 144506 (2017).

39. Dhiman, I. et al. Visualization of magnetic domain structure in FeSi based high permeability steel plates by neutron imaging. *Mater. Lett.* **259**, 126816 (2019).

40. Backs, A. et al. Universal behavior of the IMS domain formation in superconducting niobium. *Phys. Rev. B* **100**, 1–7 (2019).

41. Brooks, A. J. et al. Neutron interferometry detection of early crack formation caused by bending fatigue in additively manufactured SS316 dogbones. *Mater. Des.* **140**, 420–430 (2018).

42. Pushin, D. A. et al. Far-field interference of a neutron white beam and the applications to noninvasive phase-contrast imaging. *Phys. Rev. A* **95**, 043637 (2017).

43. Sarenac, D. et al. Three phase-grating moiré neutron interferometer for large interferometer area applications. *Phys. Rev. Lett.* **120**, 113201 (2018).

44. Kim, Y., Kim, J., Kim, D., Hussey, D. S. & Lee, S. W. Feasibility evaluation of a neutron grating interferometer with an analyzer grating based on a structured scintillator. *Rev. Sci. Instrum.* **89**, 33701 (2018).

45. Seki, Y., Shinohara, T., Ueno, W., Parker, J. D. & Matsumoto, Y. Effect of upstream beam collimation on neutron phase imaging with a Talbot-Lau interferometer at the RADEN beam line in J-PARC. *Phys. B Condens. Matter* **551**, 512–516 (2018).

46. Kim, Y., Kim, J., Hussey, D. S., Kwon, O. Y. & Lee, S. W. Visualization of magnetic domains in electrical steel using high-resolution dark-field imaging. *Korean* **57**, 352–359 (2019).

47. Kim, Y., Valsecchi, J., Kim, J., Lee, S. W. & Strobl, M. Symmetric Talbot-Lau neutron grating interferometry and incoherent scattering correction for quantitative dark-field imaging. *Sci. Rep.* **9**, 1–10 (2019).

48. Strobl, M. et al. Achromatic non-interferometric single grating neutron dark-field imaging. *Sci. Rep.* **9**, 19649 (2019).

49. Reimann, T. et al. The new neutron grating interferometer at the ANTARES beamline: design, principles and applications. *J. Appl. Crystallogr.* **49**, 1488–1500 (2016).

50. Kottler, C., David, C., Pfeiffer, F. & Bunk, O. A two-directional approach for grating based differential phase contrast imaging using hard x-rays. *Opt. Express* **15**, 1175 (2007).

51. Jensen, T. H. et al. Directional x-ray dark-field imaging. *Phys. Med. Biol.* **55**, 3317–3323 (2010).

52. Zanette, I. et al. Speckle-based x-ray phase-contrast and dark-field imaging with a laboratory source. *Phys. Rev. Lett.* **112**, 253903 (2014).

53. Marathe, S. et al. Probing transverse coherence of x-ray beam with 2-D phase grating interferometer. *Opt. Express* **22**, 14041 (2014).

54. Malecki, A. et al. X-ray tensor tomography. *EPL* **105**, 38002 (2014).

55. Harmon, K. J., Bennett, E. E., Gomella, A. A. & Wen, H. Efficient decoding of 2D structured illumination with linear phase stepping in x-ray phase contrast and dark-field imaging. *PLoS ONE* **9**, 87127 (2014).

56. Kallon, G. K. et al. A laboratory based edge-illumination x-ray phase-contrast imaging setup with two-directional sensitivity. *Appl. Phys. Lett.* **107**, 204105 (2015).

57. Morimoto, N. et al. Two dimensional x-ray phase imaging using single grating interferometer with embedded x-ray targets. *Opt. Express* **23**, 16582 (2015).

58. Morimoto, N. et al. Design and demonstration of phase gratings for 2D single grating interferometer. *Opt. Express* **23**, 29399 (2015).

59. Sharma, Y. et al. Trochoidal X-ray vector radiography: directional dark-field without grating stepping. *Appl. Phys. Lett.* **112**, 111902 (2018).

60. Shi, X. et al. Circular grating interferometer for mapping transverse coherence area of X-ray beams. *Appl. Phys. Lett.* **105**, 041116 (2014).

61. Kagias, M., Wang, Z., Villanueva-Perez, P., Jefimovs, K. & Stampanoni, M. 2D-omnidirectional hard-X-ray scattering sensitivity in a single shot. *Phys. Rev. Lett.* **116**, 093902 (2016).

62. Kagias, M. et al. Diffractive small angle X-ray scattering imaging for anisotropic structures. *Nat. Commun.* **10**, 5130 (2019).

63. Jahns, J. & Lohmann, A. W. The Lau effect (a diffraction experiment with incoherent illumination). *Opt. Commun.* **28**, 263–267 (1979).

64. Jensen, T. H. et al. Directional x-ray dark-field imaging of strongly ordered systems. *Phys. Rev. B* **82**, 214103 (2010).

65. Andersson, R., Van Heijkamp, L. F., De Schepper, I. M. & Bouwman, W.G. Analysis of spin-echo small-angle neutron scattering measurements. *J. Appl. Crystallogr.* **41**, 868–885 (2008).

66. Brown, D. & Kienzle, P. Neutron activation and scattering calculator (2015).

67. Kaestner, A. P. et al. The ICON beamline A facility for cold neutron imaging at SINQ. *Nucl. Instruments Methods Phys.* **659**, 387–393 (2011).

68. Grünzweig, C., Frei, G., Lehmann, E., Kühne, G. & David, C. Highly absorbing gadolinium test device to characterize the performance of neutron imaging detector systems. *Rev. Sci. Instrum.* **78**, 053708 (2007).

69. Morgano, M. et al. Unlocking high spatial resolution in neutron imaging through an add-on fibre optics taper. *Opt. Express* **26**, 1809 (2018).

Acknowledgements

Author contributions
J.V., R.P.H., Z.W., and M.K. conceived the experiments with support from C.G. and M.S.; J.V., R.P.H., A.K., Z.W., and M.K. conducted the experiments; Z.W., K.J., and M.K. designed and fabricated the gratings; J.V. and P.T. acquired the SEM images; J.V., C.C., M.S., and M.K. analyzed the results; J.V. and M.K. jointly wrote the manuscript with contributions from all authors.

Competing interests
The authors declare no competing interests.

Additional information